JOURNAL OF PROPULSION AND POWER
Vol. 14, No. 5, September–October 1998

Experimental Investigation of Shear Coaxial Cryogenic Jet Flames

S. Candel,* G. Herding,† R. Synder,‡ P. Scouflaire,§ and C. Rolon¶
École Centrale Paris, Châtenay-Malabry, F-92295, France
L. Vingert,** M. Habiballah,** F. Grisch,** M. Péalat,** and P. Bouchardy**
ONERA, Palaiseau 91120, France
and
D. Stepowski,†† A. Cessou,‡‡ and P. Colin§§
Université de Rouen, Mont St. Aignan 76821, France

This paper reports results from experiments carried out on the jet flame formed from a single coaxial injector. This device was fed with liquid oxygen and gaseous hydrogen and placed in a chamber equipped with quartz windows. The flame is observed with a set of optical methods: light emission from OH radicals, laser-induced fluorescence of OH and O_2, elastic, and Raman scattering from the liquid-oxygen jet. These techniques are used to obtain images of the flame zone. It is then possible to deduce the flame location with respect to the liquid jet from simultaneous elastic scattering and laser-induced fluorescence of OH measurements. Average emission images treated with Abel's transform provide the local volumetric light emission from OH radicals. This yields the mean flame structure and constitutes a different method for locating the flame. The images obtained by exciting the fluorescence of O_2 provide complementary information on the flame shape and they may be used to estimate the local reaction rate. Quantitative temperature measurements based on coherent anti-Stokes Raman scattering from H_2 give additional clues on the combustion zone. These data may be used to develop a unified picture of the flame in the vicinity of the injection plane.

Nomenclature

Da_c	=	chemical Damköhler number
Da_v	=	vaporization Damköhler number
E	=	mixture ratio
f	=	laser pulse frequency, Hz
I_j	=	intensity of the jth rotational Q line, W m^{-2}
J	=	momentum flux ratio
$\dot{m}$	=	mass flow rate, g s^{-1}
p	=	pressure, N m^{-2}
Re	=	Reynolds number
T_{GH_2}	=	inlet gaseous hydrogen temperature, K
T_{LOX}	=	inlet liquid oxygen temperature, K
T_r	=	optical filter transmission ratio
t_m, t_c, t_v	=	mechanical, chemical, and vaporization times, s
v_{GH_2}	=	inlet gaseous hydrogen velocity, m s^{-1}
v_{LOX}	=	inlet liquid oxygen velocity, m s^{-1}
v', v''	=	vibrational levels
We	=	Weber number
X	=	mole fraction
ω	=	angular frequency, rad s^{-1}

Received Sept. 2, 1997; revision received Feb. 2, 1998; accepted for publication March 2, 1998.

*Professor, EM2C Laboratory, CNRS. Member AIAA.
†Ph.D. Student, EM2C Laboratory, CNRS; currently Research Engineer, Abt. K-EFAE, Volkswagen, Wolfsburg 38436, Germany.
‡Research Scientist, EM2C Laboratory, CNRS.
§Engineer, EM2C Laboratory, CNRS.
¶Professor, EM2C Laboratory, CNRS.
**Research Scientist.
††Director of Research, CORIA, CNRS.
‡‡Research Scientist, CORIA, CNRS.
§§Ph.D. Student, CORIA, CNRS; currently Postdoctoral Fellow, DLR, German Aerospace Research Center, Hardthausen 74239, Germany.

I. Introduction

COMBUSTION in liquid rocket motors poses difficult technological problems and raises important scientific questions that have been extensively investigated in the past. Specific aspects of central interest relate to flow management, injection optimization, ignition, flame stabilization, chamber-wall cooling, dynamic response to perturbations, and combustion instabilities. Standard practice in the design of space propulsion systems has mostly relied on accumulated know-how, lessons learned, and trial-and-error methodologies.

More recently, computational tools have been progressively introduced in the design process but they have not replaced testing. Combustion in rocket motors is so complex that its computation cannot be carried out without extensive validation based on detailed investigation of the process in well-controlled configurations. The main objective of the present research program has been to generate a fundamental understanding of the combustion mechanisms and to develop an experimental database providing guidelines for computer modeling.

Results reported in this paper were gathered by different teams working in a cooperative research program on combustion in liquid rocket motors. This collaboration is sponsored by Centre National d'Études Spatiales (CNES) and Société Européenne de Propulsion (SEP) and involves ONERA and Centre National de la Recherche Scientifique (CNRS). Experiments are carried out on the Mascotte facility operated by ONERA. Data gathered in this framework are shared among the different groups. This paper includes selected samples of results obtained with light emission, elastic scattering, and laser-induced fluorescence (LIF) imaging as well as temperature measurements by coherent anti-Stokes Raman scattering (CARS). The data set is broad but still not complete. Velocity and turbulence data are not available but would have considerable value. Measurements of the liquid mass fraction would also be useful in assessing the evolution of the spray. Although

information is still missing it is nevertheless possible to propose a description of the flame structure in the near field of the coaxial injector. The present analysis is also founded on papers containing additional information: The mean flame structure is discussed in Herding et al.,[1] cryogenic flame patterns and effects of operating parameters are analyzed in Snyder et al.,[2] and flame stabilization is investigated in Herding et al.[3,4] and Stepowski et al.[5] A discussion of optical diagnostics applicable to cryogenic combustion studies is included in Brummund et al.[6] Among the many studies focusing on liquid propellant injection and combustion, those of Pal et al.,[7] Vogel,[8] and Mayer and Tamura,[9] and Mayer et al.[10] are of direct interest. Atomization in coaxial geometries are analyzed by Eroglu et al.[11] and Farago and Chigier.[12] Many aspects of spray combustion are reviewed by Faeth[13] and Sirignano et al.[14] Other references to previous literature may be found in these papers.

This paper begins with a brief review of the fundamental mechanisms controlling cryogenic flames. The Mascotte experimental facility is described in Sec. III. Diagnostics are reviewed in Sec. IV. A selected set of experimental results is provided in Sec. V together with discussions of the structure of flames formed by shear coaxial injectors.

II. Combustion Mechanisms in Cryogenic Flames

In standard applications of cryogenic combustion, reactants are introduced in the chamber through coaxial injectors. Liquid oxygen (LOX) generally flows in the inner tube at low speed while gaseous hydrogen (GO_2) is fed by the outer annular duct. In standard devices the central tube is set in recess with respect to the exhaust plane. In some devices a certain amount of swirl is also communicated to the LOX stream. In the present case we only consider flush-mounted LOX and hydrogen ducts and there is no swirl. Cryogenic combustion involves a variety of coupled physical and chemical processes that are summarized schematically in Fig. 1.

Atomization starts at the confluence of the liquid and gaseous streams. The liquid core size diminishes progressively as the spray is formed. Initial LOX ligaments are torn away by the high-speed hydrogen stream. The ligaments break into finer droplets that may still be too large to sustain the shearing stresses associated with the velocity difference between the gaseous and liquid phase. This leads to secondary atomization. The droplets vaporize and the GO_2 and gaseous hydrogen (GH_2) react in a highly turbulent flowfield.

While these processes are closely coupled one may determine several controlling factors. It is first concluded from experiments on atomization in coaxial geometries[15] that the jet breakup is sensitive to J and that the droplet size is set by the relative We_l, respectively, defined by

$$J = \frac{\rho_g v_g^2}{\rho_l v_l^2} = \frac{\text{Gas momentum flux}}{\text{Liquid momentum flux}} \tag{1}$$

$$We_l = \frac{\tau}{(\sigma/d_l)} = \frac{\rho_g (v_g - v_l)^2 d_l}{\sigma} = \frac{\text{Stresses caused by relative motion}}{\text{Surface tension forces}} \tag{2}$$

In principle, the Weber number should be calculated in terms of local quantities like the local velocity difference. However, these variables are not known and one may instead use an initial Weber number based on the injection values of velocity, surface tension, and characteristic dimension. The Reynolds numbers of GH_2 and LOX $Re_g = \rho_g v_g (d_g - d_l)/\mu_g$ and $Re_l = \rho_l v_l d_l/\mu_l$ define the initial states of flow. If these numbers are sufficiently large, the two propellant streams are turbulent and the breakup of the liquid jet depends mainly on J. This ratio controls the stripping of the liquid core and sets the core length. Studies carried out by Rehab et al.[16] indicate that the core length is inversely proportional to $J^{1/2}$. The size of the droplets formed by the primary and secondary atomization is then determined to a great extent by the Weber number.

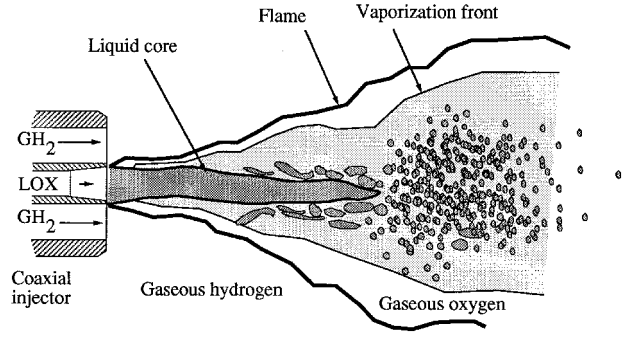

Fig. 1 Basic processes of cryogenic combustion.

Processes of vaporization, mixing, and combustion may be characterized by their characteristic times t_v, t_m, and t_c. These three characteristic times define two Damköhler numbers, a chemical reaction Damköhler number that compares the mixing time with the chemical time

$$Da_c = \frac{t_m}{t_c} = \frac{\text{Mechanical time}}{\text{Chemical reaction time}} \tag{3}$$

and a vaporization Damköhler number that compares the mixing time with the vaporization time

$$Da_v = \frac{t_m}{t_v} = \frac{\text{Mechanical time}}{\text{Vaporization time}} \tag{4}$$

Estimates of these numbers (see, for example, Snyder et al.[2]) indicate that the chemical Damköhler number is always much larger than unity, whereas the vaporization Damköhler number is generally lower than unity. It is then concluded that vaporization of the liquid droplet controls the combustion process. If the droplets produced by atomization are too large, their typical time will be excessive and the droplets might even escape the combustion chamber without being fully vaporized. The large chemical Damköhler number indicates that combustion will take place in thin reactive layers and that the regime of combustion will be of the flamelet type.

Straightforward calculations,[2] assuming that spray formed after jet breakup is monodisperse and that the droplets have the same velocity and use the observed size of the flame, provide an estimate of the ratio of the interdroplet distance b to the droplet diameter a. One finds that the spray formed after jet breakup is quite dense with droplets separated from each other by less than 10 mean diameters. Under these circumstances the regime of reaction will be dominated by external group combustion, whereby the flame is established as an outer layer surrounding the spray.

Many other parameters will influence the flame stabilization, spreading, and structure. The injector geometry and in particular a recess of the LOX tube modifies conditions at the flame edge in the stabilization layer and the subsequent flame-spreading angle. The pressure changes the rates of reaction and vaporization-inducing variations of the flame volume. Transcritical mechanisms are also significant when the chamber pressure exceeds the LOX critical pressure.

III. Experimental Facility

The Mascotte facility that is developed and operated by ONERA allows studies of elementary processes involved in cryogenic propellant combustion. The combustion chamber is equipped with a single-element combustor fed by LOX and GH_2. Three successive versions of this test facility were devised:

1) The first version (V01) featured a low-pressure chamber (<10 bar) and used hydrogen at room temperature.

Table 1 Definition of operating conditions

Point	Pressure, bar	T_{CH_4}, K	$\dot{m}_{LOX}$, g/s	$\dot{m}_{CH_4}$, g/s	v_{LOX}, m/s	v_{CH_4}, m/s	E	J	$We \times 10^3$
A	1	289	50	15.0	2.23	893	3.3	13.4	27.1
C	1	289	50	10.0	2.23	628	5.0	6.3	12.6
A-10	10	289	50	23.7	2.23	308	2.1	14.5	28.2
C-10	10	289	50	15.8	2.23	207	3.2	6.5	12.6
D′-5	5	289	40	11.2	1.78	292	3.6	10.2	12.6
C′-8	8	289	50	9.5	2.23	163	5.3	3.2	6.5
F1	1	94	50	9.5	2.23	419	5.3	8.1	16.9

2) The second version (V02) was equipped with a heat exchanger for GH_2 cooling to 100 K. This allowed an increase of the maximum flow rate of GH_2 delivered at low pressure.

3) The third version (V03) is now operating at supercritical pressures in the combustor with an increased maximum LOX flow rate (up to 400 g s^{-1}). Results described in this paper were obtained with V01 and V02.

A. Cryogenic Combustion Facility

LOX is stored in a 180-l tank pressurized with helium to minimize pollution of the liquid with dissolved gas. The LOX issued from the tank flows through a liquid nitrogen heat exchanger and reaches a temperature of 80 K to avoid vaporization and cavitation in the line and two-phase flow in the injector. During the initial chilling phase of the line, the oxygen circulation is diverted to a heat exchanger where it is vaporized before evacuation to the atmosphere. The hydrogen storage comprises two containers of 28 bottles pressurized at 200 bars, each container representing 252 m^3 of hydrogen under normal conditions. The flow rate is regulated by means of a sonic throat. A liquid nitrogen line is used to cool the combustor head and the final section of the LOX line.

Version 02 includes an additional heat exchanger in the high-pressure segment of the hydrogen line (on the upstream side of the sonic throat). The temperature can be brought down to 100 K. The mass flow rate specification may then reach 100 g s^{-1}.

The chamber pressure is limited to 10 bar in V01 and V02. The LOX and GH_2, mass flow rates for V01 range from 20 to 100 g s^{-1} for LOX and from 5 to 20 g s^{-1} for GH_2 at room temperature and at atmospheric pressure in the chamber. The upper limit of hydrogen flow rate corresponds to the sonic limit, i.e., $M = 1$ at the injector exhaust. This limit is a function of the injector geometry, the hydrogen injection temperature, and the chamber pressure. The actual upper limit of hydrogen flow rate that the test bench could deliver is related to the pressure of the storage (maximum 200 bar) and to the cross section of the sonic throat placed in the line. With the current storage of 500 m^3, the maximum available flow rate of hydrogen would be approximatively 75 g s^{-1}. On the LOX side, the i.d. of the line is 10 mm. The maximum mass flow rate corresponding to a velocity of 5 m s^{-1} in this line would be approximately 450 g s^{-1}.

B. Combustion Chamber

The combustion chamber is designed for 30 s of operation at a pressure of 1 bar, for a maximum LOX flow rate of 120 g s^{-1} at a mixture ratio of 6. This test duration is reduced to 20 s at 10 bar. It may be fired 6–10 times in a day, with 5–10 min between two successive runs. The chamber section is square with an inner dimension of 50 mm. The stainless-steel structure holds two lateral fused silica windows (100 mm long and 50 mm high). The window internal face is cooled by a gaseous helium film. The mass flow rate of helium is negligible and does not perturb the main flow. Upper and lower windows 100 mm long but only 10 mm wide are used for laser sheet transmission. The combustor is composed of different interchangeable modules, which permit visualizations of the whole combustion chamber by placing the transparent module at different longitudinal positions. The nozzle is made of graphite. A water-cooled copper nozzle is also available. The combustor has been run more than 1000 times (including 30-s runs at atmospheric pressure and 20-s runs at 10 bar). In these tests the LOX mass flow rate was varied from 40 to 90 g s^{-1}, and the GH_2 mass flow rate from 10 to 30 g s^{-1}.

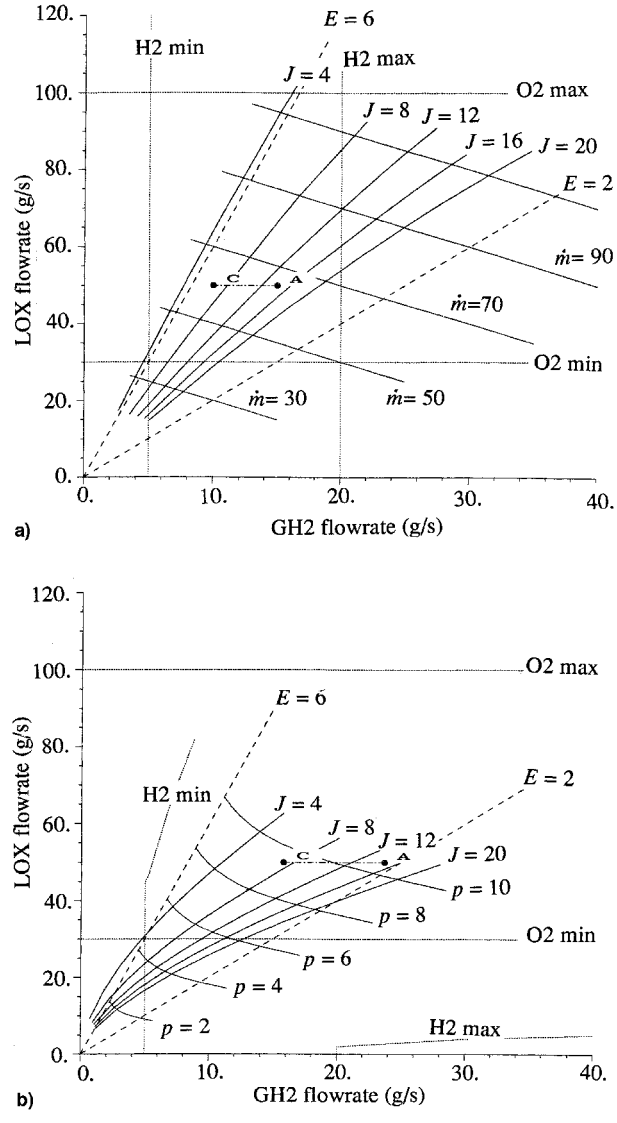

Fig. 2 Operating domains of the Mascotte facility. p = a) 1 and b) 10 bar.

C. Selection of Operating Points

The similarity between low-pressure experiments and high-pressure rocket chamber operation is not readily assured. Among the many possible scaling rules one may, however, choose to conserve the gas-to-liquid momentum ratio that essentially controls jet breakup and atomization. This choice is based on cold-flow tests reported by Hopfinger and Lasheras[15]

and by older correlations devised for shear coaxial injectors. The value of this scaling parameter is also confirmed by the set of experiments described in Ref. 2. The operating mass flow rates of LOX and GH_2 are chosen to preserve the momentum flux ratio at the different operating pressures. This in turn induces changes in the mixture ratio $E = \dot{m}_{LOX}/\dot{m}_{GH_2}$. Such variations are, however, admissible if the Da_c lies in the proper range, a condition that is well satisfied as Da_c is much greater than unity for global mixture ratios exceeding 2 ($E > 2$). Test conditions corresponding to operation at 1 and 10 bar are summarized in Table 1. In general, conditions A and C are described in this paper. Point A corresponds to a high value of the momentum ratio, whereas point C features a low value of this factor. We also give some data collected at point D' at 5 bar, point C' at 8 bar, and point $F1$ corresponding to a hydrogen injection temperature of 94 K.

It is interesting to place the main points of operation (A and C) in ($\dot{m}_{GH_2}$), $\dot{m}_{LOX}$) diagrams. These diagrams also show the available flow rates for both propellants, the mixture ratio limits, total injected mass flow rate contours (Fig. 2a) or pressure contours (Fig. 2b), as well as momentum ratio isocontours (J = *cste*).

IV. Diagnostics

A. Emission Imaging

The emission of OH radicals may be used to locate regions of intense combustion. Radiation from OH takes place in the near-uv range between 306 and 320 nm.[17] Emission bands are clearly separated from those of oxygen and water. Detection is achieved with an intensified charge-coupled device (CCD) camera (featuring 578 × 384 pixels with 12-bits depth) equipped with a Nikon 105 mm Π= 4.5 uv objective. A UG-5 glass filter blocks radiation above 400 nm and two WG 305 filters suppress radiation below 283 nm while passing 55–80% of the light emitted between 306 and 320 nm where chemiluminescence is observed. The camera is placed on one side of the combustor at right angles with respect to the axis (the setup is shown in Ref. 2). Emission images provide the instantaneous signal integrated over the line of sight (LOS), i.e., over a line orthogonal to the axial direction. It is not possible to deduce the local values from an observation under a single viewing angle. However, the instantaneous images may be averaged and the resulting data may be processed through an Abel transform to determine the mean volumetric light intensity distribution.[4] This type of numerical tomography is suitable if the flame is axisymmetric and if self-absorption of the light radiated by the flame is not too large. Rotational symmetry of the flame is not exactly verified because the flow is confined by a chamber with a square cross section. One expects, however, that the distorsion associated with the corner vortices will remain small, allowing application of the Abel transform. The second condition is also approximately satisfied in the present experiments.

B. Elastic Light Scattering

Direct illumination of liquid–gas interfaces produces elastic light scattering (ELS). Detection of ELS may then be used to locate the liquid phase and more specifically determine the distance of LOX jet breakup. A laser sheet is used as incident light while the scattered radiation is recorded with a CCD camera placed at right angles.

C. Planar Laser-Induced Fluorescence of OH

Fluorescence of OH radicals is being used extensively in combustion experiments to characterize reactive layers in flames. The pumping laser wavelength is most commonly tuned to the Q_1 branch of the rotational level $J'' = 6$ transition $A^2\Sigma(v' = 1) \leftarrow X^2\pi(v'' = 0)$ at 283.92 nm. The choice of the $J'' = 6$ level minimizes the temperature dependence of the fluorescence signal. For moderate laser intensities the regime is linear and it may then be shown that the fluorescence signal is proportional to the number density of OH molecules. In practical applications, it is convenient to detect off-resonance light radiation. The shift between the pumping wavelength and the laser-induced fluorescence (LIF) signal allows separation of the useful signal from other radiations. This is particularly important here because the LOX jet and spray produce an intense scattered signal at the pumping wavelength.

The laser pulse is generated by a Nd:YAG pumped dye laser (Continuum Powerlight and ND6000). Typical pulse energies using R590 dye and a doubling crystal were 30 mJ for a pulse duration of 20 ns. Fluorescence is detected by a gated intensified CCD camera (578 × 384 pixels with 12-bits depth) equipped with one UG-5 glass filter and four WG-305 filters that eliminate most of the scattered light. The exposure time is 50 ns, images are acquired at 10 Hz. Some Raman signal originating from the liquid phase (at 296 nm) may still be present in the detected signal but its level of 10–20% of the fluorescence signal is sufficiently low to allow interpretation of the data (see Snyder et al.[2] for details on this issue).

In some experiments two cameras were employed to obtain simultaneous images of the LOX jet (ELS) and of the flame (using LIF). After correction for orientation and scaling the images were combined to locate the flame with respect to the liquid phase. This simultaneous imaging method is also useful in evaluating possible cross talk between light scattering and LIF.

D. Planar LIF of O_2

Planar LIF (PLIF) of O_2 is well suited to investigations of cryogenic jet flames owing to its very high sensitivity at elevated temperatures. It is practically insensitive to collisional quenching up to 15 bars as the fluorescence yield is dominated by predissociation. At a given temperature the fluorescence intensity is directly proportional to the oxygen concentration and to the local laser irradiance in the control volume. The effective absorption cross section of a broadband argon–fluoride laser and the fluorescence efficiency are strongly increasing with the oxygen temperature.[18] As a drawback to this useful feature the local effective irradiance is progressively attenuated as the laser progresses in hot oxygen. Complex iterative techniques involving both temperature and concentration are usually required to correct this decay. In the present configuration, where O_2 is inside the flame, the laser irradiance will not be altered when reaching the reaction zone in which the hot and weak amount of O_2 about the stoichiometric surface can be detected with a maximum sensitivity. This reverse configuration (compared to the standard case where oxidizer is diffusing from the outside ambient air) is a key point of the detection technique that allows restoration of the flame surface (Guerre et al.[19]).

The pulsed radiation (λ = 193 nm, $\Delta\lambda \simeq 0.7$ nm, W = 170 mJ/15 ns, and f = 10 Hz) of an ArF laser (Lambda Physik LPX 100) is focused into a vertical light sheet (30 mm high × 800 μm thick) passing through the jet axis. The fluorescence is imaged at 90 deg onto a gated intensified CCD camera (Proxitronic, $\Delta t_{gate} \simeq 50$ ns) with a 105 mm Π4.5 uv objective lens equipped with a high-pass filter [T_r(193 nm) = 10^{-8}, T_r(220 nm) = 0.4], rejecting the parasitic elastic scattering at the laser wavelength. The video signal is digitized by a frame-grabber board (512 × 512 pixels on 8 bits) connected to a personal computer.

With the ArF excimer laser O_2 is excited through the Schumann–Runge system ($B^3\Sigma_u^- - X^3\Sigma_g^-$). Five vibrational bands of O_2 are present within the laser wavelength ($v' = 0 \leftarrow v'' = 4$), ($v' = 1 \leftarrow v'' = 7$), ($v' = 2 \leftarrow v'' = 10$), ($v' = 3 \leftarrow v'' = 14$), and ($v' = 3 \leftarrow v'' = 15$), which are hot bands. In our configuration excitation with the ArF excimer laser sheet allows one to map gaseous oxygen above 800 K.

E. Coherent Anti-Stokes Raman Spectroscopy

Studies carried out during the last 15 years indicate that broadband Coherent Anti-Stokes Raman Spectroscopy (CARS)

has the appropriate temporal and spatial resolutions for measurements in turbulent combustion systems. Its use in cryogenic combustion is quite challenging. CARS is observed when three waves of frequencies, ω_0, ω_1, and ω_2, pass through a gas mixture, e.g., Ref. 20. If the frequency difference $\omega_1 - \omega_2$ is close to the Raman-active vibrational frequency ω_P of a molecular component of the gas, an intense beam with frequency $\omega_3 = \omega_0 + (\omega_1 - \omega_2)$ will be generated in the forward direction of the incident waves. The two coherent incident waves ω_1 and ω_2 force the molecules to oscillate in phase at the frequency $\omega_1 - \omega_2$. Then the ω_0 radiation is scattered off by molecules whose polarizability is modulated by the oscillation. A new coherent wave is thus created at the frequency $\omega_3 = \omega_0 + (\omega_1 - \omega_2)$, called the anti-Stokes frequency. The same wave is often used to pump and probe the molecular oscillation ($\omega_0 = \omega_1$), the anti-Stokes frequency is then given by $\omega_3 = \omega_1 + (\omega_1 - \omega_2)$. A CARS spectrum, i.e., the energy of the anti-Stokes pulses as a function of the frequency difference $\omega_1 - \omega_2$, allows the chemical and temperature analysis of the gas mixture. It is created by a single laser pulse exciting one or more molecular species of the gas mixture using a broad-spectral-bandwidth ω_2 laser and detecting the resulting anti-Stokes beam with a CCD detector set up at the output of a spectrometer. The shape and the amplitude of a spectrum depend on the temperature and the density of the species, respectively. While the shape is not disturbed by thermally induced refractive index gradients affecting the beams when they pass through a turbulent medium, the amplitude is often reduced because the beams fail to cross in the prescribed probe volume. As a consequence, the first goal of CARS tests conducted on Mascotte focused on thermometry, using H_2 that is the major diatomic species present in the gas flow. The CARS setup[21] consists of an ensemble including the two lasers, their associated optics, and a detection part divided into reference and measuring channels. An optical bench of 150×50 cm^2 holds the two lasers. The ω_1 beam is the doubled-frequency output of a Nd:YAG laser chain composed of a single-mode Q switched oscillator followed by an amplifier. It is partly used to pump a dye laser chain (dye: LDS 698), which emits the broad ω_2 spectrum. The ω_2 bandwith is 100 cm^{-1} [full width at half maximum (FWHM)] and the central wavelength is 683 nm. At the output of the emitter bench, the ω_1 beam has already been split in two parallel beams and one of them is overlapped with the ω_2 beam (planar BOXCARS arrangement).[20] The energy/pulse of the beams are 30 mJ for each of the ω_1 beams and 2 mJ for the ω_2 beam. All beams are horizontally polarized. The beams are focused first in a 1-atm pressure slow flow of argon, where a weak CARS signal is created to monitor the fluctuations of direction and pulse energy of the ω_1 and ω_2 lasers and of the spectral shape of the ω_2 laser. That reference signal is then split-off and the laser beams pass to the Mascotte facility, where they are refocused in the chamber. Three pairs of 25-mm-diam, 8-mm-thick optical windows have been specially installed on the top and bottom of the burner, replacing the long and narrow ones used for the LIF laser sheet. The windows are 400–700 nm antireflection coated on their external surface and they are recessed from the chamber by 30 mm to lengthen the distance between the windows and the laser focus to avoid laser damages. The CARS beams are focused using a 140-mm-focal-length achromat yielding a 0.9-mm-long and 40-mm-diam probe volume. Reference and sample CARS spectra are then dispersed in two separate spectrometers and detected with intensified 532-photodiode arrays. The spectral dispersion is 0.25 cm^{-1}/diode and the resolution is 1.6 cm^{-1} (FWHM). The rate of data acquisition is 5 Hz.

V. Experimental Results

A. Emission, ELS, and OH–PLIF Imaging

Systematic experiments carried out on the Mascotte facility have provided a large database of images for a set of operating conditions. Some of these data are already described in Snyder et al.[2] and Herding et al.[1,3] A selection of images is included in this subsection. In the emission images included in Fig. 3 the injector geometry is shown to scale and the complete height of the chamber is displayed. It is important to remember that the signal detected by the camera is integrated over the LOS and it is therefore not possible to determine the precise nature of the patterns appearing in these pictures. It is, however, clear that radiation from OH starts right at the injector lips. The reactive layer is nearly cylindrical initially and expands farther downstream. The boundary of emission images move away from the axis and the flame fills the central portion of the chamber.

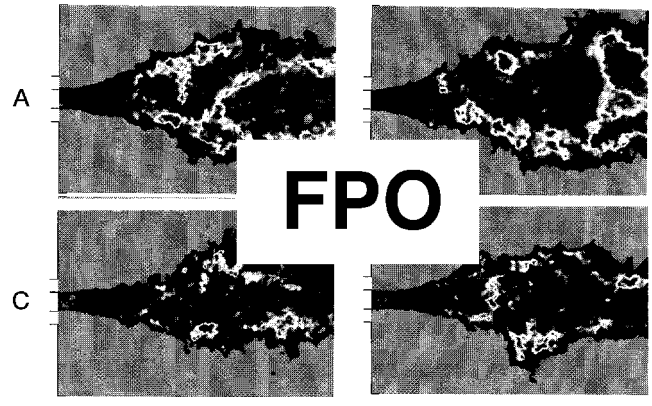

Fig. 3 Typical emission images. Radiation of OH radicals in the uv range. Exposure time Δt = 10 μs. Operating conditions A-10 and C-10. p = 10 bar.

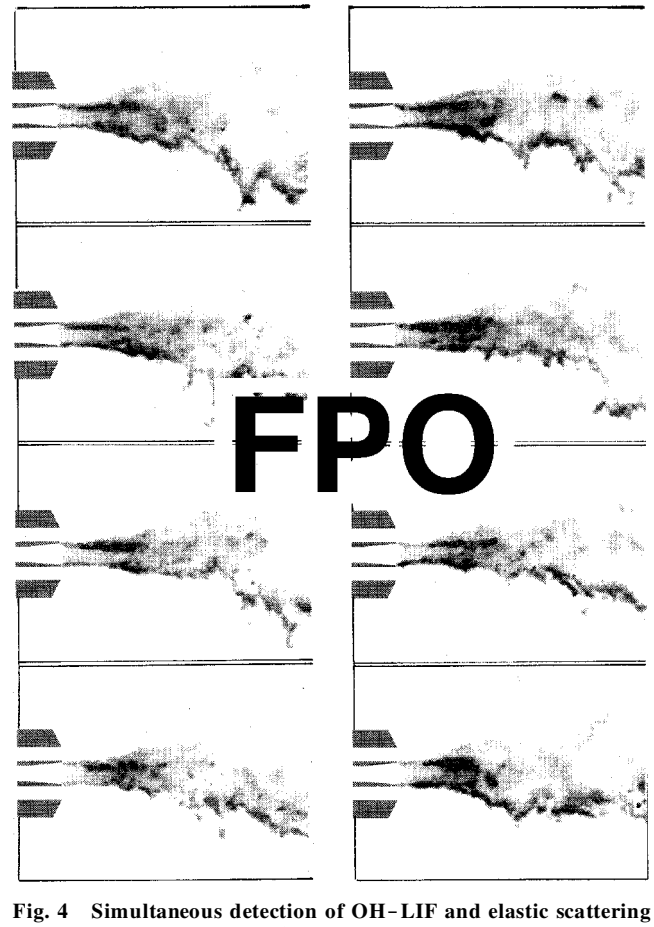

Fig. 4 Simultaneous detection of OH–LIF and elastic scattering images. Operating point: D', p = 5 bar. The background is white, elastic scattering signals are shown in blue, OH–LIF signals are displayed in red.

Combined LIF and ELS images are displayed in Fig. 4. These photographs show that the LIF signal is distinct from the scattered light. The LIF signal is already quite strong at the injector and the level does not change notably downstream. A highly corrugated layer of intense fluorescence is observed in these photographs. Near the injector the LIF and ELS signals are quite close, indicating that the flame develops in the near vicinity of the LOX core. The previous data clearly show that reaction begins near the injection plane and that the reactive layer is thin and relatively smooth initially. It becomes highly corrugated after jet breakup. The flame expands away from the axis when the spray is formed a few diameters from the injection plane. The upper trace of LIF fades out because the laser sheet is dispersed by the LOX jet and droplet cloud. The presence or absence of LIF signals on the upper side of the chamber may be interpreted by considering the quality of LOX core disintegration and atomization. If this process is delayed the laser sheet crosses the LOX jet without much distorsion and produces OH fluorescence. This is the case in the injector vicinity. If the jet breaks up and produces a dense spray of droplets, the beam is scattered effectively and cannot produce fluorescence from the upper flame sheet. This explains why the LIF signal is in general much stronger in the lower side of the chamber that is illuminated by the unperturbed laser sheet.

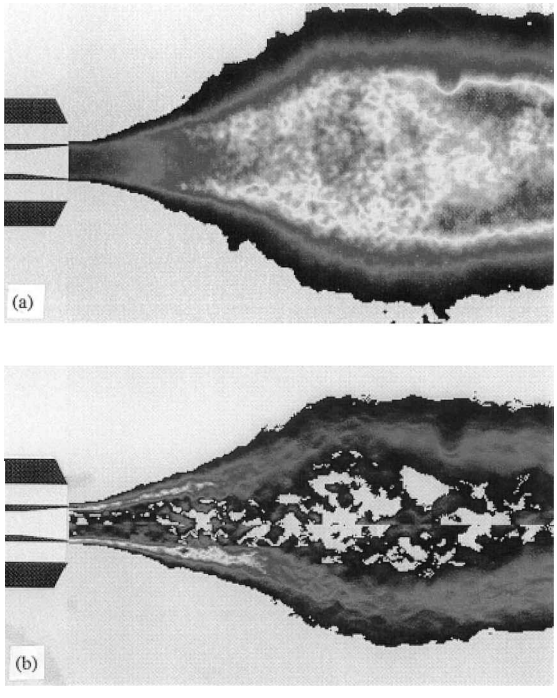

Fig. 5 Average emission image a) and Abel-transformed emission image b) for operating point A-10, p = 10 bar.

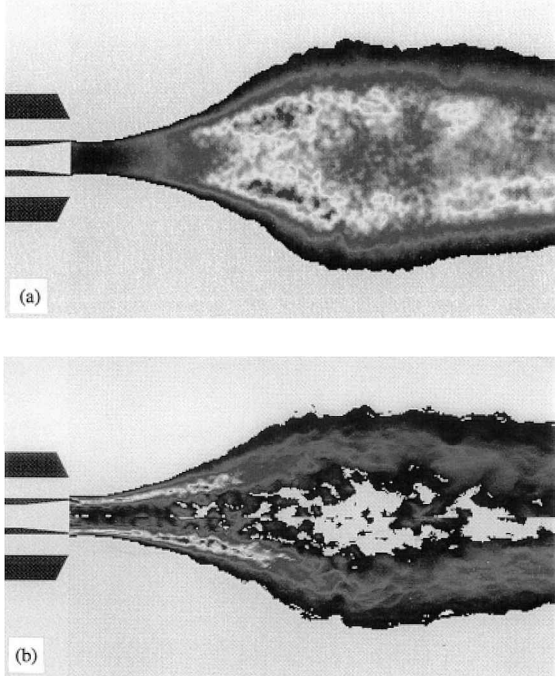

Fig. 6 Average emission image a) and Abel-transformed emission image b) for operating conditions C-10, p = 10 bar.

This general picture is confirmed by the data deduced from the Abel-transformed average emission images. Figures 5 and 6 give the emission image transformed for two operating conditions. The Abel transform is applied separately to the upper and lower sides of the image. The resulting images are therefore not quite symmetrical with respect to the axis. When comparing the two sides of the Abel-transformed images it is then possible to have an indication of the statistical variability of this processing technique. The mean volumetric distributions deduced by numerical inversion indicate that the mean flame begins at the LOX tube lip. The mean reaction zone is initially a thin, nearly cylindrical surface, which expands downstream into a thick shell surrounding the GO_2 and LOX spray formed after jet breakup. The volumetric OH emission intensity is spread over a region of finite thickness. Farther downstream the mean flame becomes annular. The inner and outer diameters of the flame volume slowly decrease with axial distance as the oxygen convected in the central region is being consumed.

B. LIF of GO_2

LIF of GO_2 has been used to map the instantaneous flame and to investigate the influence of pressure and temperature of the fast hydrogen coflow on the flame front structure. The emphasis was put on the oxygen consumption within the flame; thus 11 operating conditions were explored keeping the mixture ratio constant with hydrogen injected at 300 K (under 1 and 8 bar) and with hydrogen at 80 K (at 1 bar). Figure 7 shows an example of a single-shot fluorescence image of O_2 at 1 bar (m_{O_2} = 50 g s^{-1}, m_{H_2} = 9.5 g s^{-1}). This image indicates that the flame is attached to the injector lips as already observed in OH spontaneous emission and OH–LIF images.

Statistical analysis has been performed by processing 200 images for each operating condition to obtain the probability distribution of the flame location. A map of this distribution is presented in Fig. 8 for three different operating conditions with the same flow rates, two with H_2 at 300 K at 1 bar and 0.8 MPa (cases C and C′-8, respectively) and one with H_2 at 80 K at 1 bar (case F1). Dimensionless numbers are outlined in Table 1. In case C the probability of flame presence has a large dissymmetry that is reduced in case C′-8, where the pressure was higher. In case F1 with cold hydrogen the distribution is nearly symmetric but the flame surface is more divergent.

C. Temperature Measurements

Instantaneous temperature measurements are deduced from a single-shot CARS spectrum of H_2, which present the sin-

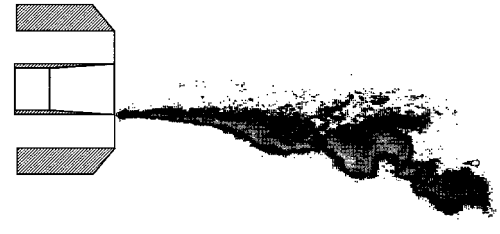

Fig. 7 Typical O_2–LIF image for combustion at 1 bar and hydrogen injected at 94 K. Operating condition F1, p = 1 bar.

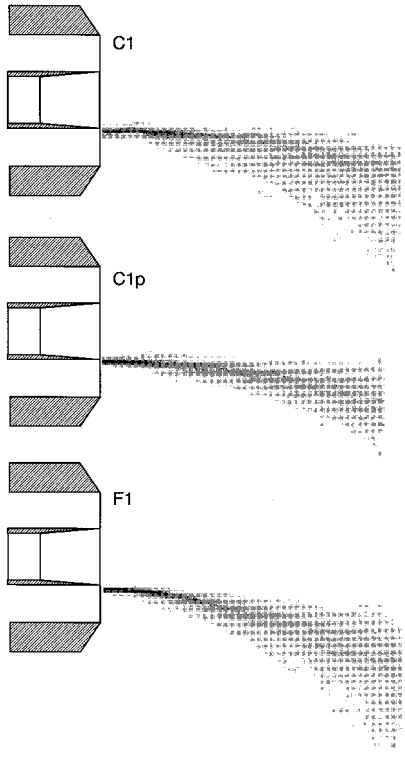

Fig. 8 Probability distribution of flame location for three operating conditions (C, C′-8, and F1).

gularity to feature a collection of isolated Q-rotational lines. At atmospheric pressure, collisional broadening is negligible and all of the lines are in the Doppler regime. Consequently, the temperatures are deduced by plotting the amplitudes of the $Q(1)$–$Q(5)$ or $Q(7)$ in a Boltzmann diagram. The error bar of an instantaneous temperature is the uncertainty given by the least-square-fitting routine and reflects the accuracy of the complete apparatus including the data processing. To illustrate the capability of the setup, an experiment is performed by feeding the Mascotte chamber with a mixture of 10% H_2 and 90% Ar. The uncertainty of the instantaneous temperatures is of the order of 10 K and the temperature averaged from 150 Boltzmann plots is 296 K with a standard deviation of 10 K. When the pressure increases, collisional processes become important and Raman linewidths of the Q-branch transitions of H_2 exhibit a well-known contraction according to an effect first analyzed by Dicke.[22] The effect, which is often termed *Dicke* or *motional narrowing*, is a result of a reduction of the Doppler contribution to the total line broadening with increasing collision frequency. The decrease in Doppler broadening results from a coherent averaging of frequencies within the normal Doppler line profile, induced by velocity-changing collisions that conserve vibrational phase. If the frequency of velocity-changing collisions is greater than that of dephasing collisions, sub-Doppler total linewidths can result. The resulting profile of the Q-rotational line is a generalized Galatry profile, where the characteristic parameters are the collisional linewidth, the Doppler linewidth, and the effective frequency of velocity-changing collisions $\beta = kT/mD$, where D is the optical diffusion coefficient. For the Mascotte experiment, the presence of H_2O and O_2, and two other possible collisional partners for H_2, contribute significantly to the H_2 relaxation processes and, consequently, also change the CARS spectral shape. H_2O has to be taken into account because of its abundance in the combustion products and the efficiency of its collision with H_2. On the contrary, the effect of O_2 is merged with those of H_2 because the collisional behavior of H_2 and O_2 are similar. Pressure-broadening coefficients for H_2–H_2 and H_2–H_2O collisions, obtained experimentally in the temperature range 300–1200 K, are extrapolated to predict the H_2 spectra at temperatures up to 3000 K. Temperatures are deduced by fitting the experimental spectra with the theoretical ones calculated for different temperatures and for different molar fractions of H_2 and H_2O. The fitting technique used is a simple least squares, where the error function is given by

$$F = \sum w_j [I_j^{\exp} - I_j^{\text{the}}(T, X_{H_2}, X_{H_2O})]^2 \tag{5}$$

where w_j is a statistical weight characteristic of the magnitude of the lines. X_{H_2} and X_{H_2O} are the molar fractions of H_2 and H_2O with $X_{H_2} = 1 - X_{H_2O}$ by assumption.

The CARS measurements correspond to four experimental conditions previously used during the LIF campaign (A and C at 1 and 10 bar).

At atmospheric pressure, the measurements are carried out at four axial locations from the injector exit (between 80 and 250 mm) by placing the combustor modules with and without optical ports as necessary. In each axial section the measurement points are located between the input window and the injector axis to reduce the disturbances affecting the beams before they reach the probe volume. An ensemble of 150 instantaneous temperature measurements are recorded during each run with an uncertainty of 50–100 K, which is 5 to 10 times more than the value obtained during the demonstration experiment. However, the temperature fluctuations induced by turbulent combustion greatly exceed this uncertainty. The measurements also show no evidence of a temperature evolution during the run indicating that the process is stationary and that

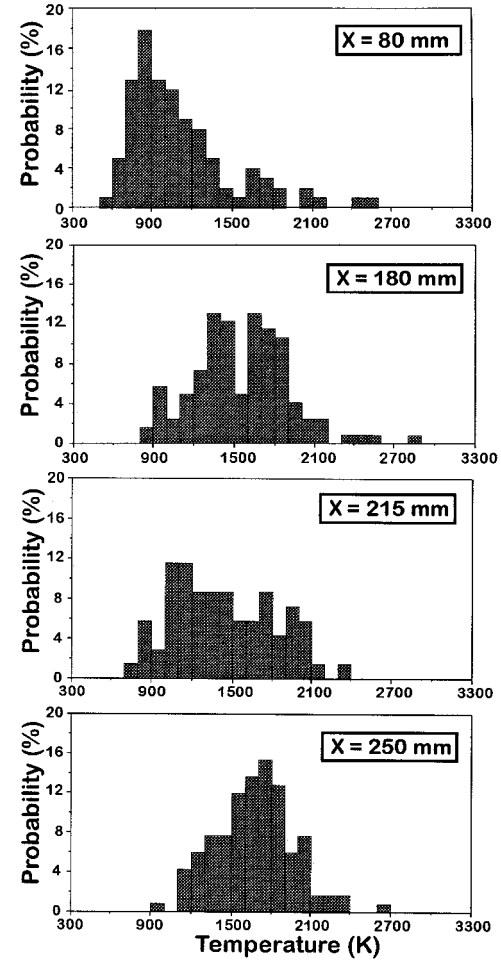

Fig. 9 CARS temperature histograms for single-shot spectra obtained at atmospheric pressure at several x positions during different runs of the combustor. Operating condition A, $p = 1$ bar. Radial position $y = 20$ mm.

it may be characterized by histograms, mean values, and standard deviations. Thus, Fig. 9 shows typical data obtained at different positions displayed with a temperature step of 100 K matching the apparatus uncertainty. The temperature distributions display the degree of burnout that depends primarily on the mixing of H_2 and O_2. Depending on the measurement locations, the validation percentage, defined as the ratio between the number of spectra successfully processed and the total number of laser pulses, ranges between 0 and 100%. Data processing fails when the experimental signals are too weak, reflecting either low instantaneous H_2 mole fraction within the probe volume or imperfect beam crossing caused by large refractive index gradients present in the chamber. Preliminary experiments devoted to probing H_2O and O_2 indicate that CARS signals could be obtained at positions where the validation rates for H_2 are too low. For $y < 10$ mm, the validation percentage is low whatever the distance from the injector because of a slow mixing of the O_2 axial flow with the surrounding H_2 flow. The mean temperature increases downstream (Fig. 10), whereas the standard deviation decreases slightly when the excess H_2 is reduced (condition C). Results show that the combustion is not complete at $x = 250$ mm when the burner operates at atmospheric pressure.

At a pressure of 10 bar the combustor runs during 15 s yielding 75 CARS data samples. Measurements correspond to sections located between 10 and 410 mm from the injector exit. Figure 11 shows the radial profiles of the mean temperature and the standard deviation of temperature at $x = 10$ mm close to the injector. No CARS signal is detected at $y = 0$ mm, indicating that hydrogen is never present in the LOX core flow. The mean temperature increases with radial distance reaching 600 K at $y = 20$ mm (condition C-10). This result indicates that hot gases formed downstream recirculate in this region. The temperature is slightly lower (by about 50 K) for operating conditions A. The temperature's standard deviation decreases with the radial distance from 120 K at $y = 5$ mm to 70 K at $y = 20$ mm, whereas the validation percentage increases from 0% at $y = 0$ mm to 90% at $y = 20$ mm. For $y > 5$ mm, the high validation rate and the low standard deviation indicate that the recirculation zone is quite homogeneous. In contrast, the low validation percentage and the large temperature standard deviation recorded at $y = 5$ mm show the presence of a zone where the H_2 mole fraction and temperature fluctuate, demonstrating the presence of an unsteady mixing layer between the inner oxygen jet and the surrounding hydrogen flow.

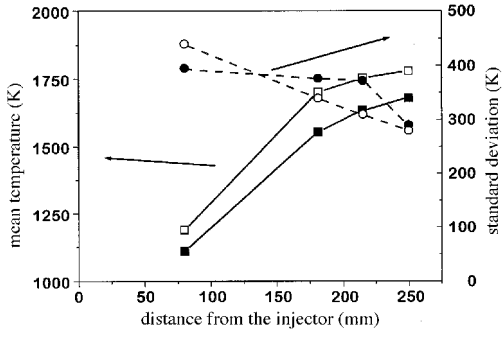

Fig. 10 Mean temperature (square symbols) and standard deviation of temperature (circles) recorded as a function of distance from the injector. Operating conditions A (black symbols) and C (open symbols). Pressure $p = 1$ bar. Radial position $y = 20$ mm.

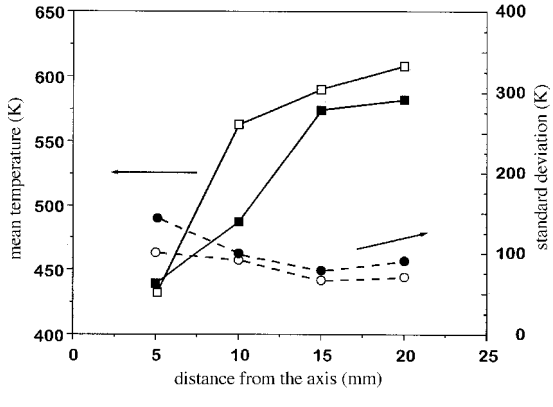

Fig. 11 Mean temperature (square symbols) and standard deviation of temperature (circles) recorded as a function of distance from the axis. Operating conditions A-10 bar (black symbols) and C-10 bar (open symbols). Axial position is $x = 10$ mm.

For the two operating conditions, radial mean temperature profiles are nearly identical. For instance, Fig. 12 shows the data recorded at three axial positions for the condition A (10 bar). The mean temperature profiles are relatively flat. The temperatures reach 2400 K with a standard deviation of about 600 K mainly because of random fluctuations induced by the turbulent flow. At $x = 180$ and 250 mm, the validation rate increases as the measurement point approaches the wall. In contrast, at $x = 410$ mm, the validation rate, nearly 50%, is constant whatever the radial position. These results lead to the following conclusions: The mean temperatures are higher (by about 300 K) than the adiabatic temperature calculated with a mixture ratio $E = 2.1$. Because the measurements require a strong CARS H_2 spectrum, there exists a potential for biasing the mean temperature; and it is expected that such biasing, when present, will be most significant in the region where the validation rate will be weak. Moreover, the precise knowledge of the collisional linewidths at high temperature may also induce an additional bias.

1) At $x = 180$ mm, the mean temperature has leveled off, indicating that intense mixing takes place in the turbulent flame.

2) At $x = 180$ and 250 mm and close to the axis, the low validation rates indicate that the hydrogen mole fraction is quite low near the inner flow. In contrast, at the chamber exhaust ($x = 410$ mm), a validation rate of about 60% for all radial positions tends to indicate that the flow is more homogeneous.

A final comparison between the mean temperature axial profiles at $y = 15$ mm recorded at 1 and 10 bar (Fig. 13) indicates that heat is released more quickly at the higher pressure.

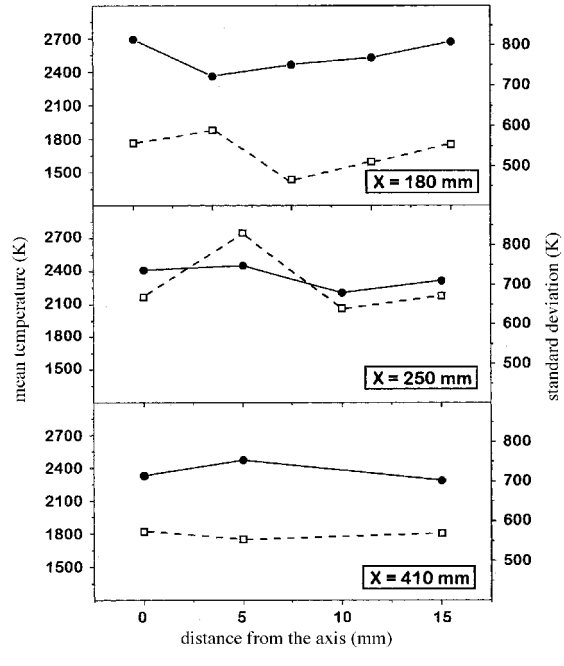

Fig. 12 Mean temperature (circles) and standard deviation of temperature (square symbols) recorded in three axial sections as a function of the distance from the axis. Operating conditions A-10, $p = 10$ bar.

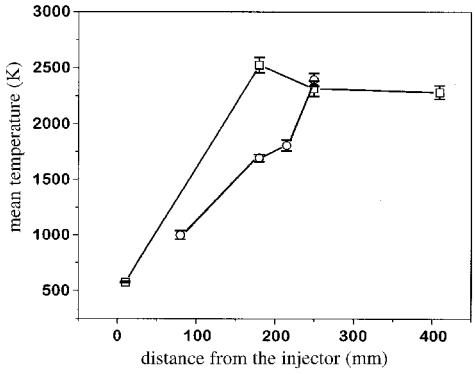

Fig. 13 Mean temperature profiles recorded as a function of distance from the injector. Operating conditions A and A-10. The circles correspond to p = 1 bar, the squares refer to p = 10 bar. The data were collected at y = 15 mm.

VI. Discussion and Conclusions

The structure of cryogenic flames is investigated in this paper. In the case of a single shear coaxial injector placed in a square chamber and for the range of parameters investigated, the flame is stabilized in the vicinity of the LOX tube and takes the shape of a shell. As indicated by the OH–PLIF images, the instantaneous reactive layer is thin and highly corrugated. The reactive sheet is initially in contact with the LOX jet and expands farther downstream. The Abel-transformed emission images show that reaction takes place in a finite region surrounding the liquid jet, and later the gaseous oxygen and LOX spray. Temperature is initially stratified in the radial direction and becomes more homogeneous farther dowstream after intense mixing.

The sharpness of the oxygen fluorescence maps support the expected assumption that the oxygen–hydrogen combustion rate is higher than turbulent mixing rate in the cryogenic jet flame. This finding is also corroborated by the fact that the flame is always attached (or nearly attached) to the lips of the coaxial injector. It is then expected that two-phase calculations and modeling based on diffusion flamelet structures can apply to this situation.

Statistics of flame location obtained from O_2–LIF show that in the near field the wrinkling and flapping of the flame are low and increase with downstream locations in agreement with the data obtained with OH–LIF and OH emission imaging.

Acknowledgments

This work was supported by SEP and CNES. Thanks go to CNES and DLR for providing a fellowship to G.H. Technical help provided by A. Mouton and R. Barrau (ONERA), Y. Le Teno, G. Lucas, and G. Coeur Joly (EM2C) is gratefully acknowledged. This work was presented at the 3rd International Symposium on Space Propulsion, Beijing, People's Republic of China, Aug. 11–13, 1997.

References

[1]Herding, G., Snyder, R., Scouflaire, P., Rolon, C., and Candel, S., "Emission and Laser Induced Fluorescence Imaging of Cryogenic Propellant Combustion," *Proceedings of the Conference on Propulsive Flows in Space Transportation Systems* (Bordeaux, France), Centre National d'Études Spatiales, France, 1995, pp. 1–14.

[2]Snyder, R., Herding, G., Rolon, C., and Candel, S., "Analysis of Flame Patterns in Cryogenic Propellant Combustion," *Combustion Science and Technology*, Vol. 124, Nos. 1–6, 1997, pp. 333–373.

[3]Herding, G., Snyder, R., Scouflaire, P., Rolon, C., and Candel, S., "Flame Stabilization in Cryogenic Propellant Combustion," *26th Symposium (International) on Combustion*, The Combustion Inst., Pittsburgh, PA, 1996, pp. 2041–2047.

[4]Herding, G., Snyder, R., Rolon, C., and Candel, S., "Investigation of Cryogenic Propellant Flames Using Computerized Tomography of OH Emission Images," *Journal of Propulsion and Power*, Vol. 13, No. 2, 1998, pp. 146–151.

[5]Stepowski, D., Cessou, A., and Goix, P., "Flame Stabilization and OH Fluorescence Mapping of the Combustion Structures in the Near Field of a Spray," *Combustion and Flame*, Vol. 99, No. 3, 1994, pp. 516–522.

[6]Brummund, U., Cessou, A., Oschwald, M., Vogel, A., Grisch, F., Bouchardy, P., Pealat, M., Vingert, L., Habiballah, M., Snyder, R., Herding, G., Scouflaire, P., Rolon, C., and Candel, S., "Laser Diagnostics for Cryogenic Propellant Combustion Studies," *Proceedings of the 2nd International Symposium on Liquid Rocket Propulsion* (Chatillon, France), ONERA, 1995, pp. 19-1–19-22.

[7]Pal, S., Moser, M. D., Ryan, H. M., Foust, M. J., and Santoro, R. J., "Drop Size Measurements in a LOX/GH2 Propellant Rocket," *Proceedings of the Central and Eastern States Sections of the Combustion Institute* (New Orleans, LA), 1993, pp. 395–399.

[8]Vogel, A., "Investigations on Atomization of a Coaxial H2/LOX Jet Under Hot Fire Conditions," *Proceedings of the 6th International Conference on Liquid Atomization and Spray Systems*, edited by A. J. Yule and C. Dumouchel, Begell House, New York, 1994, pp. 742–749.

[9]Mayer, W., and Tamura, H., "Propellant Injection in a Liquid Rocket Oxygen/Gaseous Hydrogen Rocket Engine," *Journal of Propulsion and Power*, Vol. 12, No. 6, 1996, pp. 1137–1147.

[10]Mayer, W., Schik, A., Schweitzer, C., and Schaffler, M., "Injection and Mixing Processes in High Pressure LOX/GH2 Rocket Combustors," AIAA Paper 96-2620, July 1996.

[11]Eroglu, H., Chigier, N., and Farago, Z., "Coaxial Atomizer Liquid Contact Lengths," *Physics of Fluids A*, Vol. 3, 1991, pp. 303–308.

[12]Farago, Z., and Chigier, N., "Morphological Classification of Disintegration of Round Liquid Jets in Coaxial Air Stream," *Atomization and Sprays*, Vol. 2, No. 2, 1992, pp. 137–153.

[13]Faeth, G.,"Structure and Atomization Properties of Dense Turbulent Sprays," *23rd Symposium (International) on Combustion*, The Combustion Inst., Pittsburgh, PA, 1990, pp. 1345–1352.

[14]Sirignano, W., Delplanque, J. P., Chiang, C. H., and Bhatia, R., "Liquid Propellant Droplet Vaporization: A Rate Controlling Process for Combustion Instability," *Liquid Rocket Engine Combustion Instability*, edited by V. Yang and W. Anderson, Vol. 169, Progress in Astronautics and Aeronautics, AIAA, Washington, DC, 1995, pp. 307–344.

[15]Hopfinger, E., and Lasheras, J. C., "Breakup of a Water Jet in High Velocity Co-Flowing Air," *Proceedings of the 6th International Conference on Liquid Atomization*, edited by A. J. Yule and C. Dumouchel, Begell House, New York, 1994, pp. 110–117.

[16]Rehab, H., Villermaux, E., and Hopfinger, E., "Flow Regimes of Large Velocity Ratio Coaxial Jets," *Journal of Fluid Mechanics*, Vol. 345, Aug. 1997, pp. 357–381.

[17]Dieke, G. H., and Crosswhite, H. M., "The Ultraviolet Bands of OH: Fundamental Data," *Journal of Quantitative Spectroscopy and Radiative Transfer*, Vol. 2, No. 2, 1962, pp. 97–199.

[18]Lee, M. P., and Hanson, R. K., "Calculations of O_2 Absorption and Fluorescence at Elevated Temperatures for a Broadband Argon-Fluoride Laser Source at 193 nm," *Journal of Quantitative Spectroscopy and Radiative Transfer*, Vol. 36, No. 5, 1986, pp. 425–440.

[19]Guerre, S., Bazile, R., and Stepowski, D., "Conditioned Dissipation and Average Consumption Maps in a Turbulent Non-Premixed Flame Using Planar Laser Induced Fluorescence of O_2," *26th Symposium (International) on Combustion*, The Combustion Inst., Pittsburgh, PA, 1996, pp. 105–111.

[20]Eckbreth, A. C., *Laser Diagnostics for Combustion Temperature and Species*, Abacus Press, Cambridge, MA, 1988.

[21]Magre, P., Moreau, P., Collin, G., Borghi, R., and Péalat, M., "Further Studies by CARS of Premixed Turbulent Flames," *Combustion and Flame*, Vol. 71, No. 2, 1988, pp. 147–153.

[22]Dicke, R. H., "The Effect of Collisions on the Doppler Width," *Physical Review*, Vol. 89, No. 2, 1953, pp. 472, 473.